Vadose Zone Journal

Testing the Fill-and-Spill Model of Subsurface Lateral Flow Using GPR and Dye Tracing

Journal:	*Vadose Zone Journal*
Manuscript ID	VZJ-2017-07-0142-FHCZ.R1
Manuscript Type:	Original Research Articles
Date Submitted by the Author:	n/a
Complete List of Authors:	Nyquist, Jon; Temple University, Earth and Environmental Science Toran, Laura; Temple University, Earth and Environmental Science Pitman, Lacey; Temple University, Earth and Environmental Science Guo, Li; Penn State Univ., Ecossytem Science and Management Lin, Hangsheng (Henry); Penn State Univ., Ecossytem Science and Management
Keywords:	Geophysics, ground penetrating radar, dye tracer, preferential flow, Critical Zone

Testing the Fill-and-Spill Model of Subsurface Lateral Flow Using GPR and Dye Tracing

Jonathan E. Nyquist[1], Laura Toran[1], Lacey Pitman[1], Li Guo[2], Henry Lin[2,3]

[1]Department of Earth and Environmental Science, Temple University, Philadelphia, USA; [2]Department of Ecosystem Science and Management, Pennsylvania State University, University Park, USA; [3]Department of Eco-Environment, Institute of Earth Environment, Chinese Academy of Sciences, Xi'an, China

Core Ideas

Lateral flow patterns revealed by dye tracing agreed with time lapse GPR data

Lateral flow varied from less than a meter to a meter at adjacent sites

3D radar detected banding in the strike direction but not dye fingering

Fractured saprock modifies the fill-and-spill model by facilitating vertical flow

Abstract

Preferential flow (PF), which bypasses large portions of the soil or subsurface matrix, is critical in the transport of water and dissolved constituents in the unsaturated zone. To test the "fill-and-spill" model of hillslope hydrology that describes the generation and pattern of downslope lateral PF after storms, we used dye tracer and time-lapse, ground-penetrating radar (GPR) on a forested hillslope in the Susquehanna-Shale Hills Critical Zone Observatory. We injected 50 L of water mixed with brilliant blue dye (4 g/L) into a shallow trench cut perpendicular to the slope and used GPR to monitor the tracer downslope across a 1.0 m × 2.0 m grid. The site was then excavated to the soil-saprock interface and photographed to document the dye pathways. We observed vertical dye fingering near the infiltration trench. Downslope lateral PF at the soil-saprock boundary was limited to ~0.40 m, which is evidence that the soil-saprock interface did not fill and spill. The extent, depth, and direction of the downslope PF indicated by GPR generally matched the dye staining patterns in the excavation, but the resolution of the 800-MHz GPR antenna was insufficient to distinguish small fingers of dye. A revised "fill-and-spill" model was proposed for this site that incorporates the PF through fractured saprock before water encounters fresh bedrock surface. This study demonstrates that GPR integrated with dye tracer infiltration can provide a useful means of testing hillslope hydrological hypothesis and unraveling the complexity of PF at the hillslope scale in the field setting.

Key words: Geophysics, ground penetrating radar, dye tracer, preferential flow, Critical Zone

Introduction

Hillslope hydrology comprises complex processes that remain poorly understood despite decades of study. Unsaturated porous media flow models are commonly used to model flow and transport despite a general realization that Richard's Equation does not capture preferential flow (PF) that is typically dominant. Beven and Germann (2013) attributed the continuing reliance on porous media flow models to the increasing availability of unsaturated, porous media, modeling software and insufficient data to parameterize PF models on the macropore scale. Burt and McDonnell (2015) suggested that the conceptual model of "fill-and-spill" (Tromp van Meerveld and McDonnell, 2006; Graham et al., 2010) may provide a better working hypothesis for hillslope runoff phenomena. The proposed mechanism is rapid infiltration of precipitation through the soil layer down to the fresh bedrock surface or other less permeable horizon followed by lateral flow along the interface, with water filling some small depressions and then overflowing down along the hillslope. Fill-and-spill behavior may also result from excess saturation causing the water table to rise into shallower transmissive layers (McDonnell, 2013). After a certain amount of precipitation reaching the ground, the fill-and-spill model predicts rapid lateral flow downslope following PF pathways controlled by the topography of the low permeability horizon and microchannels above the bedrock (Graham et al., 2010). The fill-and-spill model has been applied to describe and predict the generation and pathways of the downslope flow above impermeable layers (e.g., the bedrock surface), flow dynamics at less permeable layers (such as the allocation of vertical percolation and downslope flow), and the threshold response of discharge to total precipitation of a hillslope (Tromp-van Meerveld and McDonnell, 2006; Graham et al., 2010).

Given the potentially broad applicability of the fill-and-spill model (McDonnell, 2013), field verification is needed. However, determining whether or not fill-and-spill is an important mechanism for lateral flow in different natural setting is challenging because instrumenting a hillside with a sufficient density of sensors to map subsurface flow networks is often impractical, and doing so would likely alter the system under study. Salve et al. (2012) instrumented a hillslope with wells for neutron probes, time domain reflectrometry, and electrical resistivity. They found bedrock wetting occurred before the saprolite was saturated, and the responses were highly heterogeneous. They also observed that the instrumentation was better at detecting wetting fronts than soil moisture values. In addition to detailed soil moisture instrumentation, predicting flowpaths for fill-and-spill requires detailed knowledge of bedrock microtopography which is buried beneath the subsurface.

Dye tracer tests remain the most direct technique for mapping PF networks, and numerous studies have demonstrated the variety and complexity of PF in natural systems (e.g., Flury et al., 1994; Flury and Flühler, 1995; Anderson et al., 2009; Wang and Zhang, 2011; Beven and Germann, 2013). Unfortunately, dye tracer tests have a limited ability to show the temporal evolution of PF process, and they require excavation, which is time-consuming. Although Anderson et al. (2009) used dye staining and excavation to trace PF pathways over a 30-m section of Russell Creek research watershed in British Columbia, Canada, it is difficult to conduct a similar experiment over an entire hillside or watershed. Furthermore, large-scale excavation irreparably destroys the natural soil fabric of the system under study, which negates the possibility of repeated studies. Consequently, there is interest in non-intrusive methods for characterizing subsurface water movement.

Geophysical imaging provides continuous, non-destructive characterization of large subsurface areas. Ground-penetrating radar (GPR) has the highest spatial resolution of all current geophysical methods and is especially sensitive to the distribution and dynamics of soil moisture. Recently, Guo et al. (2014) imaged lateral PF networks on a hillslope in the Susquehanna Shale Hills Critical Zone Observatory (SSHCZO) using time-lapse common offset GPR. In their experiment water was introduced into a trench cut perpendicular to the hillslope and GPR data were collected at regular time intervals before, during, and after infiltration along a series of transects downslope that were parallel to the trench. Their analysis of changes in radar data showed only localized changes in reflection amplitude. They did not see any large-scale changes in the radar velocities affecting the time/depth alignment of the radar traces, therefore they were able to compare time-lapse radargrams using direct subtraction. They attributed the small, radargram amplitude changes to PF confined to a series of macropore conduits above a dense layer, which they could trace downslope by connecting the changed areas on successive radargrams. Data from moisture sensors at the soil pit face that was 0.5 m downslope of the radar grid were consistent with their proposed explanation for the temporal evolution of the changes in the radar data, but in the absence of direct ground truth data within the radar grid, their interpretation remains somewhat speculative. In fact, it remains challenging to map and monitor subsurface flow at the field scale (Allaire et al., 2009; Angermann et al., 2017), making the verification of the flow patterns derived from the GPR data fairly difficult. Consequently, in most of the previous applications of GPR to investigate subsurface flow, ground truth of the flow pathways, such as by dye staining, is generally lacking (e.g., Truss et al., 2007; Doolittle et al., 2012; Zhang et al., 2014).

Therefore, to further demonstrate and validate the application of GPR technology in subsurface flow investigation, a direct comparison between the GPR derived and the actual flow patterns is required. Our objective was to partially replicate the experiment performed by Guo et al. (2014) with the addition of brilliant blue dye to the water release and subsequent excavation to compare changes detected using 3D, time-lapse GPR with PF patterns mapped by dye-tracing and excavation. Then, the effectiveness of time-lapse GPR to detect and locate flow pathways was evaluated, in particular to distinguish closely located flow pathways and to map the direction of flow pathways. To our best knowledge, this is the first time that time-lapse GPR was compared with dye staining to characterize subsurface flow dynamics in the field. Moreover, we hypothesized that the "fill-and-spill" model may be in effect for portions of the SSHCZO, mainly along planar hillslopes and near ridgetop areas where depth to bedrock is shallow. Previous studies conducted in the same catchment have shown that for some storm events water arrives more quickly at depth via lateral PF routes (Lin and Zhou, 2008; Graham and Lin, 2011). We further hypothesized that 3-D GPR could be used to map the shallow bedrock microtopography in sufficient detail to delineate fill-and-spill pathways.

Methods

Site Description

Our study site was located on the south-facing backslope side of the SSHCZO (Figure 1), which is part of the forested Shaver Creek Watershed located 24 km south-southwest of State College, Pennsylvania. The SSHCZO is one of ten CZOs funded by the National Science Foundation (NSF). A humid, temperate forest, roughly 110 years old, comprised of largely deciduous trees with some conifers covers the watershed (Naithani et al., 2013). The region is underlain by the Silurian age Rose Hill Formation, which consists of sequences of olive-colored

shale, grey siltstones, and red hematite sandstone that were deposited in marine or brackish-water environments (Folk, 1960). At our site, the Rose Hill is present as a shale composed primarily of illite (58 wt. %), quartz (30 wt. %), and vermiculated chlorite (11 wt. %), plus trace amount of feldspar, anatase, Fe-oxides and zircon (Brantley et al., 2016). The bedrock is highly fractured, with folded and faulted layers NE-SW (N54^{o}W), dipping 25^{o}-76^{o} to the NW (Jin et al., 2010).

Jin et al. (2011) made the distinction between bedrock, saprock and regolith, using "bedrock" to refer to chemically unaltered parent rock. "Saprock" is fractured and chemically altered, but competent to the extent that it must be drilled to obtain samples. "Regolith" has been disaggregated, highly altered, and can be sampled using a hand auger. In our study, we excavated using hand tools, thus we removed soil and regolith to expose the saprock surface but not true bedrock.

Previous work at the study site has revealed lateral flow of a meter or more based on geophysical monitoring during injection tests. Two injection experiments were conducted at a site 10 m upslope from the present study area. One injection was monitored with soil moisture sensors and GPR (Guo et al., 2014), which suggested lateral flow as far as 1.3 to 1.8 m downslope. The second experiment was monitored with electrical resistivity tomography and showed an increase in soil moisture 1.3 m downslope (Lichtner et al., 2012). These experiments were in part motivation for the present more detailed survey, where we have added dye injection followed by excavation. A site approximately 10 m downslope from the earlier studies was selected for excavation.

Dye Injection

154 The dye tracer was released in trench dug perpendicular to the hillslope and 0.2 meters
155 upslope of the first radar line. The trench was 1.15 m long, 0.20 m wide, and 0.18 m deep. Water
156 and dye were added to the trench by pumping into a 1.15 m long PVC pipe with a horizontal slot
157 running its length to ensure even dispersal along the trench, which was maintained at a constant
158 ponding depth of 10 cm in the infiltration trench during the infiltration experiments (Figure 2).
159 The bottom of the infiltration trench was located within the Bw horizon. Two injections were
160 conducted on the July 18th, 2013, which was in the dry period of the Shale Hills catchment with a
161 soil moisture content of ~15% m^3m^{-3} on the planar hillslope (Naithani et al., 2013). No rainfall
162 events were recorded during one week before the experiment. A total of 53 L of water was first
163 injected to wet the soil, then a second injection was performed using 53 L of water mixed with
164 Brilliant Blue dye at a concentration of 4 g/L (Petersen et al., 2001; Wang and Zhang, 2011).
165 Addition of the dye increased the conductivity of the solution, which measured 3 mS/cm. The
166 injection volume was based on the previous experiment at the site, which resulted in downslope
167 travel of approximately 2 m along preferential flow paths. The first infiltration took 10 minutes
168 and the second 27 minutes.

169 Monitoring Using Time-Lapse Ground Penetrating Radar

170 Numerous studies have investigated GPR as a tool to map moisture (see Huisman et al.,
171 2003; and Grote et al., 2013 for reviews). For typical GPR systems with a fixed
172 transmitter-receiver offset, the goal is to map reflections. GPR radar energy is reflected at
173 boundaries between layers with contrasting dielectric properties:

174

$$R = \frac{\sqrt{\varepsilon_2} - \sqrt{\varepsilon_1}}{\sqrt{\varepsilon_2} + \sqrt{\varepsilon_1}}, \quad (1)$$

175

where R is the reflection coefficient, and ε_1 and ε_2 are the dielectric constants in media 1 and 2, respectively. Topp et al. (1980) developed an empirical relationship between soil water content and dielectric constant:

$$\theta = 4.3\times10^{-6}\varepsilon^3 - 5.5\times10^{-4}\varepsilon^2 + 2.92\times10^{-2}\varepsilon - 5.3\times10^{-2}, \quad (2)$$

where θ is the volumetric soil water content (m^3/m^3). Because most geologic materials have relative dielectric constants in the range of 3-30, compared with a dielectric constant of 81 for water (Reynolds, 1997), even small changes in saturation over time will alter radar reflection patterns significantly. Using GPR to detect PF pathways by mapping soil moisture changes requires comparing GPR images of before and after events. However, detection of moisture changes by direct subtraction time-lapse radargrams is an inherently unstable process (Versteeg and Birken, 2000) because changes in soil moisture alter the propagation velocity of the radar waves in addition to the amplitude of the radar reflections. Velocity changes shift locations of the reflections on the radargram, and these shifts accumulate with depth, causing artifacts on the differenced radargram below the area of actual moisture change because of misalignment the before and after radargrams (Truss et al., 2007). Because our experiment focused on only the top half-meter of the subsurface, travel times were short and this misalignment was minor.

Our GPR survey grid covered an area 2 m wide perpendicular to the hillslope by 1 m parallel to the hillslope. For each radar survey, we collected data over a 3D grid comprised of 21 lines, each 2 m long, spaced 0.05 m apart. For time-lapse GPR it is of paramount importance that the data collection be as reproducible as possible to avoid introducing artifacts on the differenced radargrams between successive GPR scans. Following the example of Haarder et al. (2011), we

constructed a wooden frame with an adjustable bar and pegs along the sides to guide the antenna along each of the lines to ensure the lines were parallel, evenly spaced, and reproducible (Figure 2). A tow rope was used to draw the antenna along the line smoothly and to reduce the amount of foot traffic on the grid. A survey wheel attached to the antenna recorded the distance along the lines. To assess reproducibility, two complete radar surveys of the grid were completed before the injection (background), after the initial release of water (post-water) and again after the release of the water and dye solution (post-dye).

We used a Mala radar system with shielded antenna operating at a center frequency of 800 MHz and a 0.14 m separation between the transmitter and receiver antennae. We collected 400 samples per trace at time step of 0.1164 nS for a total record length of 46.434 nS. The traces were triggered every centimeter along the 2-m lines. Data collection for all 21 lines took approximately 15 minutes.

The radar velocity was calibrated after the tracer experiments by hammering a steel rod parallel to the surface into the excavated wall along the soil-saprock interface at a known depth, running a radar line over the rod, and picking the arrival time in the resulting radargram. This velocity was used in subsequent time to depth conversion, but the assumption of a uniform, constant velocity must be considered approximate because of the heterogeneity of the soil and changes in moisture content during the experiments.

GPR processing

Post-processing of the radar data comprised the following steps: (1) Removal of the DC component by detrending, dewow filtering to remove low-frequency noise, (2) first-arrival time zero adjustment, (3) low-pass filtering to remove frequencies above 1600 MHz (4) background removal by subtraction of the average trace for each line to remove antenna reverberation, (5)

trimming of data below 15 nS, which corresponded to signal degraded by attenuation in the shale saprock beneath the regolith, (6) inverse amplitude gain, and (7) time to depth conversion using a constant velocity of 0.077 m/nS. Because of velocity heterogeneity and perturbations created by the water release we chose not to migrate the data. Guo et al. (2014) refined the algorithm of Boschetti et al. (1996) to align the first breaks of the traces. That proved unnecessary for our data as the slow, gentle movement of the antenna during data collection and the use of a frame to guide the radar antenna yielded data with no noticeable trace-to-trace time shifts and repeat traces along the line matched within a centimeter. The gain function we used was inverse amplitude decay, which computes the best fitting exponential of the form to the mean trace (Tzanis, 2010). We calculated the decay curve using data for the first line of the background survey (closest to the trench), and then applied the same gain to all lines for consistency when calculating temporal changes. All the standard processing steps were conducted using matGPR (Tzanis, 2010), a freeware package written as a toolbox for Matlab (MATLAB, 2015), which was also used to difference the radargrams to highlight temporal changes. The choice of differencing schemes and alternatives will be discussed in the results section as it is data set dependent.

The processed and differenced 2D time-lapse radargrams were then loaded into GPR-Slice v7.0 (Goodman, 2015), a processing package designed for 3D visualization of GPR data. The data were first aggregated into 20 horizontal time slices spanning 4.3 nS, with 50% overlap between slices, to cover the full 15 nS region of interest. The data within each time slice were interpolated to fill the gaps between the radar lines on a grid cell size of 1 cm using inverse distance squared weighting. Then the time slices were interpolated vertically to complete the 3D grid used for visualization.

Excavation

After the tracer experiments and GPR surveys were complete, the soil and regolith were excavated to expose and document PF pathways, and to compare with the interpretation of the time-lapse GPR data. The excavations were performed manually using shovels, trowels, and a pickaxe once the saprock was reached. The excavation started 0.20 cm downslope of the injection trench to preserve the stability of the excavation wall and prevent accidental contamination by the heavily dyed soil in the trench. To document the vertical and lateral change in PF pathways, the soil was excavated in a series of horizontal layers at depths of 0.05 m, 0.08 m, 0.25 m, and 0.38 m, then photographed. Excavation ceased in the downslope direction once the dye no longer stained the soil and bedrock.

Identification of dye-stained pixels

The procedure to identify dye-stained areas within an excavation can range from purely qualitative – separating stained from non-stained soil based on visual inspection and investigator judgement – to quantification of dye concentration from the soil color (Persson, 2005). The latter requires high-quality camera equipment, careful color correction of the photographic images for white balance, exposure settings, and uneven illumination in the field. In addition, laboratory analysis of soil samples must be performed to develop a soil-specific, calibration curve for color versus concentration. We opted for a qualitative approach, but one that is independent of the observer, by using a k-means unsupervised clustering algorithm to classify the pixels as either stained or unstained.

The RGB color values are first converted into the L*a*b* color space (Baldevbhai and Anand, 2012), also known as the CIELAB, 1976, color space. In this color space, the L-axis ranges from light to dark, the a-axis from red to green and the b-axis from blue to yellow. Thus,

all of the chromicity information is contained within the a-b plane, independent of pixel brightness. The L*a*b* color space has the further advantage of perceptual uniformity. A change of the same amount at any point along any axis should produce an equivalent change in human perception, an approach pioneered in the development of the Munsell color system.

K-means clustering (Jain, 2010) is then applied to the pixels values in the a-b plane, so they are grouped by color independent of illumination. The K-means algorithm is an unsupervised classification algorithm; the operator does not provide any a priori information about which pixels are stained. The input parameters are: a distance measure, the number of clusters, k, and initial seed points for each of the k clusters. The algorithm then seeks to divide the dataset into the k clusters comprised of pixels that are closer to the mean of each cluster than the means of neighboring clusters. As a distance measure, we chose the commonly used Euclidean distance as measured in the a-b color plane. The number of clusters is chosen to be the minimum where dye-stained pixels are not lumped with other color changes, such as soil horizon boundaries. This required minimum number of clusters will be site-dependent. The initial cluster seeds are chosen randomly, but running the clustering algorithm repeatedly with different seed points (we chose n=6), mitigates the danger that the solution will converge to a local minimum. The color conversion and k-means analysis were performed using Matlab, and examples of the procedure are provided in software's documentation (MATLAB, 2015).

Infiltration experiment at secondary site

An additional infiltration experiment was performed on a nearby hillside (Figure 1) in the same formation where the soil had been removed for road aggregate, exposing the saprock. Water was poured on the exposed saprock surface through a perforated pipe to create a line source. The wetted surface was photographed to show where lateral flow and infiltration

occurred relative to the exposed fractures on the saprock surface. Water was also directly poured on exposed fractures and infiltration rates were timed. This simple experiment was used to provide direct observation of the relationship between fracture patterns and lateral flow and additional ground truthing for the infiltration experiment.

Results and Discussion

Excavation and Saprock Infiltration

Dye was not visible in the O or A horizons (a total of ~5 cm thick). At a depth of 7-8 cm, a finger of dye was located in the center part of the excavated area, centered on a root that had a diameter of 2 cm, which indicated a PF pathway along a root channel. Deeper excavation showed that the dye was no longer centered on this root. However, near the center of the excavation pit, two large fingers of dye (~15 cm × ~12 cm) were exposed, roughly 15 cm apart, that started at the base of several roots. Furthermore, the two largest roots were located above the two largest dye plumes. Relic bedding planes were observed below the roots, and the dye stained the surface of the bedding planes. The bedding planes were oriented 33° off strike from the injection trench, which had a strike of 269°.

By the time the excavation had reached a depth of 0.25 m distinct fingers of dye were apparent, two of which are visible in Figure 3. It was clear that the dye infiltration was at least partially controlled by the relict bedding. At the base of the excavation pit, the widths of the dye fingers increased. From the injection trench to the end of the dye stained area, the extent of lateral flow was ~0.40 m. The dye traveled more than 0.38 m in the vertical direction and faded rapidly beyond this depth over most of the horizontal plane of excavation (Figure 3). Some dye was observed on the left side (looking upslope) below this plane, but the total depth of penetration was not measured because manual excavation of saprock was not feasible. The total

314 excavated volume stained with dye was 0.4 m downslope by 0.65 m wide × 0.35 m deep. From a
315 simple mass balance calculation (multiplying the observed volume stained by dye times porosity),
316 we can deduce that for a porosity of 45%, one third of the dye solution infiltrated the saprock
317 instead of flowing laterally along the soil-saprock boundary. Although the estimation of the
318 visible dye area is rough, the selected porosity is overly conservative. Lower porosities would
319 require even more infiltration to explain the limited extent of lateral flow.

320 The heterogeneous nature of the saprock was revealed in the infiltration experiment at the
321 nearby hillside where saprock was exposed. Water poured on the saprock surface followed
322 surface topography for several meters, crossing bedding planes, but infiltrated once it
323 encountered a permeable fracture. Later, some isolated wet areas appeared several meters
324 downslope from where the water had infiltrated, forming return flow (Figure 4). The saprock
325 fractures are in part the result of repeated freeze-thaw cycles (Jin et al., 2010). Fractures of this
326 origin close at depth, and when they filled with water, the decrease in permeability with depth
327 could create return flow. Water poured directly on fractures showed that a fracture set with 10 m
328 spacing had higher infiltration rates than other fractures, including fracture intersections. The
329 experiment also pointed out that not all fractures lead to infiltration, which helps explain
330 previous experiments nearby in the Shale Hills study site that showed more lateral flow than the
331 trench excavated here. This experiment showed PF pathways along horizontal fissures in saprock
332 that conducted water the downslope in addition to vertical infiltration through the fractured
333 saprock

334 *GPR differencing*

335 Determining temporal changes by simple radargram differencing is an inherently unstable
336 process (Versteeg and Birken, 2000) because changes in soil moisture change the velocity of

radar wave and create a phase misalignment between the before and after radargrams. We investigated several techniques to compensate the phase shift between the radargrams collected before and after the tracer release, such as dynamic time warping (Hale, 2013; Nyquist et al., 2014), and complexity-invariant distance measures (Batista et al., 2014). We did not see a significant improvement over direct differencing of the radargrams imaging of the areas with soil moisture changes, so we elected to use the simplest approach — direct subtraction of the corresponding background survey line. In our experiment, the addition of the tracer solution principally changed the radar reflection amplitudes. While velocity changes associated with water retention in the upper half-meter created some cumulative delay, it did not cause enough phase shift to obscure the changes apparent in the differenced radargrams.

Comparison of the same radar line extracted from the two separate background surveys showed that the heterogeneous structure of the soil was closely reproduced. There were slight changes in the reflections energies between the two surveys, so differencing did not result in complete cancelation, yielding instead a fainter ghost image of the original structure. The degree of cancelation varied from line to line and along a given line, likely the result of small changes in antenna angle and coupling with ground surface during the data collection. A sample trace selected from the center of the first line from both background surveys further illustrated the reproducibility of the data (Figure 5).

The before, after, and differenced radargrams for the line closest to the trench (20 cm away) for the water release with no dye added shows changes in the reflection amplitudes (Figure 6). The GPR survey line is centered on the trench, which extends from 0.5-1.5 m, and the reflection amplitudes have changed in a roughly corresponding zone, with a disturbance width that increases with depth. There is an indication of asymmetry, with more of the change

occurring between 0.4 and 1.0 m than between 1.0 and 1.4 m, which is consistent with the dip of the relic bedding and dye staining pattern seen in Figure 3.

The same line after the dye release (Figure 7) shows a similar pattern with a slight increase in the magnitude of the change in reflection amplitude. This reflectivity increase is the opposite of what was reported by Haarder et al. (2011) who found a radar response weakened by signal attenuation in zone of dye infiltration, which they attributed to the elevated conductivity of dye solution. There are two competing factors at work here: signal enhancement by the increased contrast between wet and dry layers, and attenuation by conductive pore fluids. Haarder et al. (2011) were studying vertical infiltration. They saturated a portion of the sediments below their grid, thus attenuation dominated. However, they reported an increase in radar reflection amplitude along the edges of the infiltration area, which they attributed to lateral flow at the edges of the wetting front. This reflectivity increase just outside the infiltration area would be where the tracer-induced moisture changes remained below saturation. We suggest that the combination of well-drained soils and slow lateral migration kept our study plot unsaturated, and that the reflectivity increases were more significant than the losses due to signal attenuation, and thus area influenced by the infiltration appeared as a zone with enhanced reflectivities.

It is interesting to compare the 3D visualization of the background GPR data (no differencing) with the excavation. In general, the data simply reflect the highly heterogeneous soil layer, with diffractions from rock fragments and no continuous reflection horizons. In the 2D radargrams it is difficult to determine the soil thickness from the radar because there is no clear reflection from the saprock (Figure 5), probably because of the gradual change in dielectric constant over this gradational boundary. Even in soil profiles it is difficult to delineate the soil-saprock interface. However, structure does emerge in the 3D radar images near the

soil/saprock interface (Figure 8). A horizontal slice through the GPR data hints at diagonal banding consistent with the strike direction of the saprock seen in the excavation. The horizontal resolution for the GPR at this depth can be estimated from the radius of the first Fresnel Zone (Reynolds, 1997):

$$r=\left(\frac{\lambda^2}{16}+\frac{\lambda z}{2}\right)^{1/2}, \quad (3)$$

where λ is the wavelength and z is the depth. At our site, this equation predicts a radius of approximately 8 cm at depth of 35 cm. Thus, the horizontal resolution is insufficient to image the bedding clearly, but apparently larger irregularities in the saprock with the same strike are visible. However, these are only visible in the horizontal slices through the 3D data, not in the individual 2D radargrams.

Horizontal depth slices through the 3D volume made from interpolation of the differenced radargrams after the water and dye solution releases clearly show the change near the infiltration trench dominated by vertical infiltration with limited lateral PF (Figure 9). The second injection doubled the amount of water released but only slightly increased the size of the plume delineated by the radar, providing further evidence that much of the fluid went into the saprock. Once infiltrated into the saprock it could not be tracked much further because of strong attenuation of the radar signal by the shale. Including the 20-cm offset between the infiltration trench and the radar grid, the total lateral flow was only about 40 cm. Comparing the dye staining pattern with images constructed by compositing horizontal and vertical slices through the radar difference volume (Figure 9) shows agreement. The pattern after the water and dye releases is similar. In both cases the extent of the changed area is limited to 30 to 40 cm from the injection trench. The excavation data are also consistent with limited lateral flow.

To compare a vertical slice through the 3D GPR data with dye staining pattern on the wall of the excavation, we used k-means clustering to classified pixels as either strained or unstained. We found four to be the minimum number of clusters required for the k-means algorithm to segment the dye stained pixels into a distinct cluster, although the white rope and the nearly white portions of the ruler were classified as part of this cluster as well because white objects have a much stronger blue component than soil. When this cluster is superimposed on the corresponding vertical slice through the 3D radar data (Figure 10 D) there is good qualitative agreement between the staining pattern and the change in the GPR data. There are no stained areas that the GPR did not detect, and the photograph of the excavation shows an unstained area on the wall near the center of the trench that matches an area of minimal change in the radar images. However, there is disagreement near the right edge, where the GPR shows change that was not seen in the dye staining of excavation.

Results from dye staining patterns and time-lapse GPR surveys suggested that there was limited fill-and-spill flow at the soil-saprock interface in the study site where vertical infiltration dominated the flow regime in the permeable saprock (Figures 8 and 9). Therefore, we proposed a refined fill-and-spill model to include PF process through fractured saprock before water encounters bedrock surface (Figure 11). As depicted in this conceptual model, precipitation rapidly infiltrates the thin soil layer and forms limited lateral PF along the regolith-saprock interface before flow converges into the fissures in saprock; then the bulk of the water infiltrates the regolith-saprock interface and percolates vertically through the fractured saprock down to unweathered bedrock surface. The infiltration in the saprock layer results in heterogeneity where nearby locations may vary in the extent of lateral flow. Furthermore, part of the water may flow downslope along the horizontal fissures and reemerge to ground surface as return flow. Once

water encounters the less permeable bedrock surface, a transient water table may form in small depressions and trigger continuous lateral PF downslope above bedrock surface; some water may percolate into the aquifer as deep drainage (Figure 11). This two layer fill-and-spill model is consistent with observations of Salve et al. (2012) that saprolite can have PF paths that transfer water to the bedrock without the saprolite wetting up. As the weathered bedrock (or saprock) is commonly present in hillslope with a thin soil cover, the refined fill-and-spill model has a potentially broader applicability to predict hillslope hydrology. Future efforts are needed to test and improve the fill-and-spill model and incorporate it into hillslope hydrology models.

Time lapse GPR could image bulk moisture changes in the shallow subsurface, but could not resolve the finer structure of fingering visible in the dye excavation at the SSHCZO. At this site, the bulk of the tracer infiltrated vertically to the regolith-saprock boundary, then rather than follow the fill-and-spill model, it simply infiltrated fractures in the saprock. This saprock infiltration was unexpected because geophysical and soil moisture probe data from similar experiments at nearby sites with deeper soils (Lichtner et al., 2012; Guo et al., 2014) showed evidence of lateral flow over at least a meter.

There is indication that the radar data could detect large heterogeneities in the flow pattern. Near the center of the survey dye solution bypassed a zone roughly 10 cm wide, and there is corresponding unchanged zone in the 3D radar image, but the resolution of the radar too low to detect finer structure. Grasmueck et al. (2005) showed that maximum detail can be resolved using “full-resolution” 3D radar collection, where the spacing between the radar lines is less than a quarter wavelength. For our site, this would have dictated a maximum line spacing of a little over a centimeter, increasing the acquisition time fivefold, requiring roughly an hour and a quarter to collect the data even for our small 1 m × 2 m grid. Thus, increased spatial resolution

would come at the cost of temporal resolution, a problem when monitoring highly dynamic processes. In the future, data acquisition time may decrease as multi-antenna radar systems are becoming increasingly available, although to the authors' knowledge none have yet been fabricated with an inter-antenna spacing as small as a centimeter. Exploring the potential benefits of full-resolution 3D GPR for imaging shallow, heterogeneous soils is a promising avenue for research.

Because the contrast created by dye staining depends on soil type and illumination, and GPR change detection depends on background noise and soil dielectric proprieties, a site-specific empirical relationship between dye concentration and GPR response would be required to choose appropriate thresholds for a statistical comparison of the size and shape of the changed regions mapped by each method. This is further complicated the different resolutions of each method. Dye pattern changes can be seen on finer scale than can be mapped by GPR. Quantitative comparison is an area for further research but is beyond the exploratory scope of this paper.

Conclusions

The model that is emerging for storm flow at the SSHCZO is more complicated than simple lateral flow along a regolith-saprock interface because of unevenly-spaced, permeable fractures and anisotropy of the underlying saprock. A refined fill-and-spill model is proposed to predict the complex hillslope hydrology of the study site, which is a typical forested hillslope with a thin soil cover and a fractured bedrock layer. Such an improved empirical understanding of subsurface hydrology can help model storm water patterns in hillslopes.

In the shallow vadose zone, dye tracer tests offer the most compelling evidence of flow pathways, but cannot be reproduced because excavation destroys the soil fabric. Geophysical techniques, such as GPR, provide a promising opportunity to map and monitor subsurface flow

pathways non-invasively and can be repeated in the field. However, due to the lack of appropriate approaches, ground truthing of subsurface flow patterns derived from the geophysical data is often lacking. Here, we demonstrated the potential of combining geophysical investigation and dye tracer tests to reveal subsurface PF in a natural hillslope. Given that the performance of geophysical techniques is highly dependent on local conditions, such as soil textures, soil wetness, subsurface anisotropy, and surface topography, we suggest conducting small-scale experiments that compare geophysical data with dye staining patterns to evaluate the accuracy of geophysical results and guide the selection of proper settings of the geophysical techniques, e.g., the antenna frequency of GPR. Then the optimized geophysical surveys can be applied to a greater spatial scale. We believe that geophysical techniques that are validated by direct ground truth can open a new window to enhance the field investigation of subsurface hydrology in future studies.

Acknowledgments

This work was facilitated by a seed grant from the National Science Foundation Critical Zone Observatory program, which funded the Susquehanna Shale Hills Observatory (SSHCZO). The SSHCZO is administered by the Pennsylvania State University under grants to Christopher J. Duffy (EAR 07-25019) and Susan L. Brantley (EAR 12-39285, EAR 13-31726). The research was conducted in Penn State's Stone Valley Forest, which is supported and managed by the Penn State's Forestland Management Office in the College of Agricultural Sciences. L.G. and H.L. are supported in part by the U.S. National Science Foundation Hydrologic Sciences Program Grant EAR-1416881 (PI: H. Lin).

References

Allaire, S. E., Roulier, S., & Cessna, A. J. (2009). Quantifying preferential flow in soils: A review of different techniques. *Journal of Hydrology*, *378*(1–2), 179–204. http://doi.org/10.1016/j.jhydrol.2009.08.013

Anderson, A. E., Weiler, M., Alila, Y., & Hudson, R. O. (2009). Dye staining and excavation of a lateral preferential flow network. Hydrology and Earth System Sciences Discussions, 13(6), 935–944. doi:10.5194/hessd-13-935-2009.

Angermann, L., Jackisch, C., Allroggen, N., Sprenger, M., Zehe, E., Tronicke, J., … Blume, T. (2017). Form and function in hillslope hydrology: Characterization of subsurface flow based on response observations. *Hydrology and Earth System Sciences*, *21*(7), 3727–3748. http://doi.org/10.5194/hess-21-3727-2017

Baldevbhai, P. J., & Anand, R. S. (2012). Color Image Segmentation for Medical Images using L*a* b* Color Space. *Journal of Electronics and Communication Engineering*, *1*(2), 24–45. http://doi.org/10.9790/2834-0122445

Batista, G. E. A. P. A., Keogh, E. J., Tataw, O. M., & De Souza, V. M. A. (2014). CID: An efficient complexity-invariant distance for time series. Data Mining and Knowledge Discovery, 28, 634–669. doi:10.1007/s10618-013-0312-3.

Beven, K., & Germann, P. (2013). Macropores and water flow in soils revisited. Water Resources Research, 49(February 2012), 3071–3092. doi:10.1002/wrcr.20156.

Binley, a., Cassiani, G., & Deiana, R. (2010). Hydrogeophysics: Opportunities and challenges. Bollettino Di Geofisica Teorica Ed Applicata, 51(December), 267–284.

Boschetti, F., Dentith, M. D, List, R. (1996). A fractal-based algorithm for detecting first arrivals on seismic traces. Geophysics, 61(4), 1095. doi:10.1190/1.1444030.

Brantley, S.L., R.A. DiBiase, T.A. Russo, Y. Shi, H. Lin, K. Davis, et al. 2016. Designing a suite of measurements to understand the Critical Zone. Earth Surf. Dyn. 4:211–235. doi:10.5194/esurf-4-211-2016

Burt, T. P., & McDonnell, J. J. (2015). Whither field hydrology? the need for discovery science and outrageous hydrological hypotheses. *Water Resources Research*, *51*(8), 5919–5928. doi:10.1002/2014WR016839.

Doolittle, J., Zhu, Q., Zhang, J., Guo, L., & Lin, H. (2012). Geophysical Investigations of Soil–Landscape Architecture and Its Impacts on Subsurface Flow. *In* Hydropedology (H. Lin editor). Elsevier. doi:10.1016/B978-0-12-386941-8.00013-7.

Flury, M., Flühler, H., Jury, W. A., & Leuenberger, J. J. (1994). Susceptibility of soils to preferential flow of water: A field study. Water Resources …, 30(7), 1945–1954. doi:10.1029/94WR00871.

533 Flury, M., & Flühler, H. (1995). Tracer Characteristics of Brilliant Blue FCF. Soil Science
534 Society of America Journal, 59(1), 22–27.

535 Folk, R. L. (1960). Petrography and origin of the Tuscarora, Rose Hill, and Keefer formations,
536 Lower and Middle Silurian of eastern West Virginia. Journal of Sedimentary Research,
537 30(1), 1–58. doi 10.1306/74D709C5-2B21-11D7-8648000102C1865D.

538 Freeland, R. S., & Odhiambo, L. O. (2006). Subsurface characterization using textural features
539 extracted from GPR data. Transactions of the ASABE, 50(1), 287–293.

540 Gish, T. J., Dulaney, W. P., Kung, K.-J. S., Daughtry, C. S. T., Doolittle, J. a., & Miller, P. T.
541 (2002). Evaluating Use of Ground-Penetrating Radar for Identifying Subsurface Flow
542 Pathways. Soil Science Society of America Journal, 66, 1620.
543 doi:10.2136/sssaj2002.1620.

544 Goodman, D. (2015). GPR-SLICE v7.0 Manual. Retrieved from:
545 http://www.gpr-survey.com/gprslice

546 Graham, C. B., & Lin, H. S. (2011). Controls and Frequency of Preferential Flow Occurrence: A
547 175-Event Analysis. *Vadose Zone Journal*, *10*(3), 816. doi:10.2136/vzj2010.0119

548 Graham, C. B., Woods, R. a., & McDonnell, J. J. (2010). Hillslope threshold response to rainfall:
549 (1) A field based forensic approach. *Journal of Hydrology*, *393*(1-2), 65–76.
550 doi:10.1016/j.jhydrol.2009.12.015

551 Grasmueck, M., Weger, R., & Horstmeyer, H. (2005). Full-resolution 3D GPR imaging.
552 Geophysics, 70(1), K12–K19. doi:10.1190/1.1852780

553 Grote, K., Anger, C., Kelly, B., Hubbard, S., & Rubin, Y. (2010). Characterization of Soil Water
554 Content Variability and Soil Texture using GPR Groundwave Techniques. Journal of
555 Environmental & Engineering Geophysics. doi:10.2113/JEEG15.3.93

556 Guo, L., Chen, J., & Lin, H. (2014). Subsurface lateral preferential flow network revealed by
557 time-lapse ground-penetrating radar in a hillslope. Water Resources Research, 50(12),
558 9127–9147. doi:10.1002/2013WR014603

559 Haarder, E. B., Looms, M. C., Jensen, K. H., & Nielsen, L. (2011). Visualizing Unsaturated
560 Flow Phenomena Using High-Resolution Reflection Ground Penetrating Radar. Vadose
561 Zone Journal, 10(1), 84. doi:10.2136/vzj2009.0188

562 Hale, D. (2013). Dynamic warping of seismic images. Geophysics, 78(2). Retrieved from
563 http://library.seg.org/doi/abs/10.1190/geo2012-0327.1

564 Huisman, J. a., Hubbard, S. S., Redman, J. D., & Annan, A. P. (2003). Measuring Soil Water
565 Content with Ground Penetrating Radar: A Review. Vadose Zone Journal, 2(4), 476–491.
566 doi:10.2113/2.4.476

Jain, A. K. (2010). Data clustering: 50 years beyond K-means. *Pattern Recognition Letters*, *31*(8), 651–666. http://doi.org/10.1016/j.patrec.2009.09.011

Jin, L., Ravella, R., Ketchum, B., Bierman, P. R., Heaney, P., White, T., & Brantley, S. L. (2010). Mineral weathering and elemental transport during hillslope evolution at the Susquehanna/Shale Hills Critical Zone Observatory. Geochimica et Cosmochimica Acta, 74(13), 3669–3691. doi:10.1016/j.gca.2010.03.036

Jin, L., Rother, G., Cole, D. R., Mildner, D. F. R., Duffy, C. J., & Brantley, S. L. (2011). Characterization of deep weathering and nanoporosity development in shale - A neutron study. American Mineralogist, 96, 498–512. doi:10.2138/am.2011.3598

Lichtner, D, Nyquist, J, Toran, L, Guo, L., Lin, H. (2012). Monitoring time-lapse changes in soil moisture during artificial infiltration with geophysical methods. Annual Meeting of Geological Society of America (Charlotte, NC) Abstracts with Programs. Vol. 44, No. 7, p.48.

Lin, H., & Zhou, X. (2007). Evidence of subsurface preferential flow using soil hydrologic monitoring in the Shale Hills catchment. *European Journal of Soil Science*, *59*(1), 34–49. doi:10.1111/j.1365-2389.2007.00988.x

MATLAB (2015). version 8.5.0.197613 (R2015a). Natick, Massachusetts: The MathWorks Inc.

McDonnell, J. J. (2013). Are all runoff processes the same? *Hydrological Processes*, *27*(26), 4103–4111. doi:10.1002/hyp.10076.

Naithani, K. J., Baldwin, D. C., Gaines, K. P., Lin, H., & Eissenstat, D. M. (2013). Spatial Distribution of Tree Species Governs the Spatio-Temporal Interaction of Leaf Area Index and Soil Moisture across a Forested Landscape. *PLoS ONE*, *8*(3), 1–12. http://doi.org/10.1371/journal.pone.0058704

Nyquist, J. E., Toran, L., Pitman, L., & Lin, H. (2014) Dynamic time warping of time-lapse GPR data to monitor infiltration at the Shale Hills Critical Zone Observatory. Symposium for the Application of Geophysics to Environmental and Engineering Problems, Boston, MA.

Nyquist, J. E., Toran, L., & Lin, H. (2015) Ground-based LiDAR mapping of infiltration and flow paths on a bedrock slope. Symposium for the Application of Geophysics to Environmental and Engineering Problems, Austin, TX.

Persson, M. (2005). Accurate Dye Tracer Concentration Estimations Using Image Analysis. *Soil Science Society of America Journal*, *69*(4), 967. http://doi.org/10.2136/sssaj2004.0186

Petersen, C. T., Jensen, H. E., Hansen, S., & Koch, C. B. (2001). Susceptibility of a sandy loam soil to preferential flow as affected by tillage. *Soil and Tillage Research*, *58*, 81–89.

Reynolds, J. M. 1997. An Introduction to Applied and Environmental Geophysics. John Wiley and Sons, Chichester, England.

602 Salve, R., Rempe, D. M., & Dietrich, W. E. 2012. Rain, rock moisture dynamics, and the rapid
603 response of perched groundwater in weathered, fractured argillite underlying a steep
604 hillslope. *Water Resources Research*, *48*(11), W11528, doi:10.1029/2012WR012583.
605

606 Topp, G. C., Davis, J. L., & Annan, A. P. (1980). Electromagnetic Determination of Soil Water
607 Content: Measurements in Coaxial Transmission Lines. Water Resources Research, 16(3),
608 574–582. Retrieved from
609 http://onlinelibrary.wiley.com/doi/10.1029/WR016i003p00574/full

610 Tromp-van Meerveld, H. J., & McDonnell, J. J. (2006). Threshold relations in subsurface
611 stormflow: 2. The fill and spill hypothesis. *Water Resources Research*, *42*(2), 1–11.
612 doi:10.1029/2004WR003800.

613 Truss, S., M. Grasmueck, S. Vega, and D. A. Viggiano (2007), Imaging rainfall drainage within
614 the Miami oolitic limestone using high- resolution time-lapse ground-penetrating radar,
615 Water Resour. Res., 43, W03405, doi:10.1029/2005WR004395.

616 Tzanis A., (2010). matGPR Release 2: A freeware MATLAB® package for the analysis &
617 interpretation of common and single offset GPR data. FastTimes 15(1), 17–43.

618 Versteeg, R., & Birken, R. (2000). Controlled imaging of fluid flow and a saline tracer using
619 time lapse and electrical resistivity tomography. In Proceedings of the Symposium for the
620 Application of Geophysics to Environmental and Engineering Problems (pp. 283–292).
621 Retrieved from http://library.seg.org/doi/pdf/10.4133/1.2922754

622 Wang, K., & Zhang, R. (2011). Heterogeneous soil water flow and macropores described with
623 combined tracers of dye and iodine. Journal of Hydrology, 397(1-2), 105–117.
624 doi:10.1016/j.jhydrol.2010.11.037

625 Zhang, J., Lin, H., & Doolittle, J. (2014). Soil layering and preferential flow impacts on seasonal
626 changes of GPR signals in two contrasting soils. Geoderma, 213, 560–569.
627 doi:10.1016/j.geoderma.2013.08.035

628

629 **Figure Captions**

630
631 Figure 1: The dye tracer test site was located on the south-facing backslope of the
632 Susquehanna-Shale Hills Critical Zone Observatory. The size of the symbol marking the
633 location of the GPR survey grid (actual size: 1m × 2m) is exaggerated for visibility. Left
634 panel shows the relative locations of the dye tracer test site and the soil borrow pit used
635 for the surface water release experiment.
636 Figure 2: Water and brilliant blue dye were pumped into a shallow trench upslope of the GPR
637 survey grid. A slotted, meter-long PVC pipe (inset) was used to ensure the tracer solution
638 was dispersed uniformly and to maintain a constant head during the injection. An
639 adjustable wooden frame acted as a GPR antenna guide to ensure reproducible data
640 collection.
641 Figure 3: The top photograph shows the excavation face near the center of the injection trench to
642 a depth of 25 cm showing two distinct fingers of dye (arrows). Rope in the photograph
643 shows the intersection of the horizontal and vertical faces. The ruler is 30.5 cm (1 ft) long.
644 The bottom photograph shows the infiltration trench and the final extent of the
645 excavation, reaching a depth of 38 cm. The red and white markings on the pole are each
646 30.5 cm long. The black box outlines the region photographed in the enlargement above.
647 Figure 4: Photograph of soil moisture revealed in the infiltration experiment along the excavated
648 dipslope (secondary site). Water moved laterally approximately 4.5 m until a PF was
649 encountered. Further lateral flow may take place through the horizontal fissures in
650 saprock and form the observed return flow at a downslope location (wet surfaces marked
651 at 2.8 m).

Figure 5: Comparison of the line closest to the injection trench from the two background surveys collected before injection, the differenced section, and center traces from both lines showing the reproducibility of the data. The first 2 nS (8 cm) have been muted to eliminate the air wave. Depth was calculated assuming a homogeneous velocity of 0.077 m/nS.

Figure 6: Comparison of the line closest to the injection trench from before and after the water injection. The differenced section shows the change starting at about 15 cm broadening with depth and trending slightly to the left, which is consistent with infiltration path seen in the excavation (Figure 3). Note that the vertical blue lines in the differenced radargram align with the ends of the injection trench with ran from 50 – 150 cm and was upslope 20 cm from this line. Change in amplitude and a slight phase shift can be seen in the sample trace from the center of the section. The first 2 nS (8 cm) have been muted to eliminate the air wave. Depth was calculated assuming a homogeneous velocity of 0.077 m/nS.

Figure 7: Comparison of the line closest to the injection trench from before and after the dye solution injection. Note that the vertical blue lines in the differenced radargram align with the ends of the injection trench with ran from 50 – 150 cm and was upslope 20 cm from this line. The change in the differenced section has slightly increased in size (compared with Figure 6). The phase shift seen in the sample trace has also increased. The first 2 nS (8 cm) have been muted to eliminate the air wave. Depth was calculated assuming a homogeneous velocity of 0.077 m/nS.

Figure 8: A horizontal slice through the 3D interpolated background GPR data at the depth of the saprock shows lineations, evidence of bedding fabric (dashed lines) that is consistent with

the orientation seen in the excavation. Rope in the photograph shows the intersection of the horizontal and vertical faces.

Figure 9: Horizontal slices from 8 to 53 cm made through the 3D volume at composited depths were constructed from the volume of radargrams collected after dye solution injection minus the background radargrams. The time window for each slice encompasses the return energy over roughly half a wavelength of GPR signal, with successive slices overlapping to show the change with depth. The scale is in squared amplitude. There is some indication of fingering in the radar slices, but blurred by lack of resolution and interpolation smoothing. The extent of lateral flow is clear. Most of the change is in the 20 cm of the radar grid closest to the injection trench. The trench was at 1.2 m in the y direction and extends 0.5-1.5 m in the x-direction, as shown for the upper-most slice in the top left.

Figure 10: The radar images are a composite of a vertical x-z slice closest to the trench (0.20 m), a horizontal x-y slice at the depth equal to the base of the excavation (0.38 m), and two vertical y-z slices at the x limits of the grid. The patterns of change after the water release (A) and the dye solution release (B) are similar. The scale is normalized to the brightest reflection. The photograph of the vertical excavation face closest to the injection trench is shown (C) with and without the k-means identification of the dye stained pixels for comparison. The pixels classified as dye stained are shown superimposed on the corresponding 3D radar collected after the dye release (D) for comparison.

Figure 11: A refined fill-and-spill model with PF processes occurring at the top of two layers, both saprock and bedrock. In a hillslope with a thin soil cover underlain by a weathered bedrock (or saprock) layer, the bulk of the precipitation rapidly infiltrates soils and

saprock and forms limited lateral PF on the soil-saprock interface. Lateral PF may take place through the horizontal fissures in saprock and form return flow at downslope. Once water encounters fresh bedrock surface, a transient water table may perch at small depressions and then triggers lateral PF downslope.

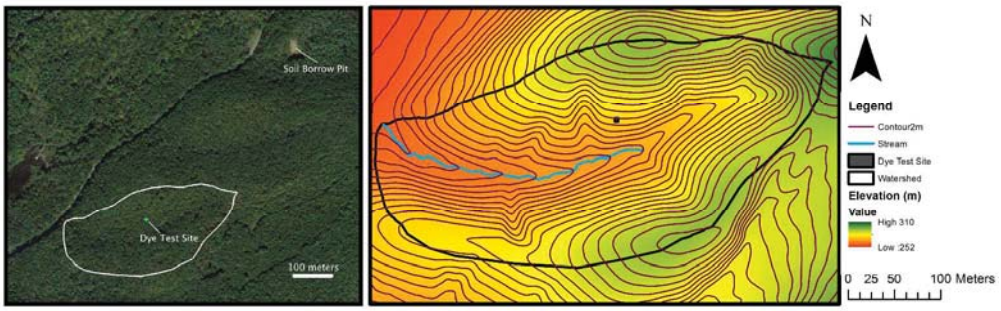

Figure 1: The dye tracer test site was located on the south-facing backslope of the Susquehanna-Shale Hills Critical Zone Observatory. The size of the symbol marking the location of the GPR survey grid (actual size: 1m × 2m) is exaggerated for visibility. Left panel shows the relative locations of the dye tracer test site and the soil borrow pit used for the surface water release experiment.

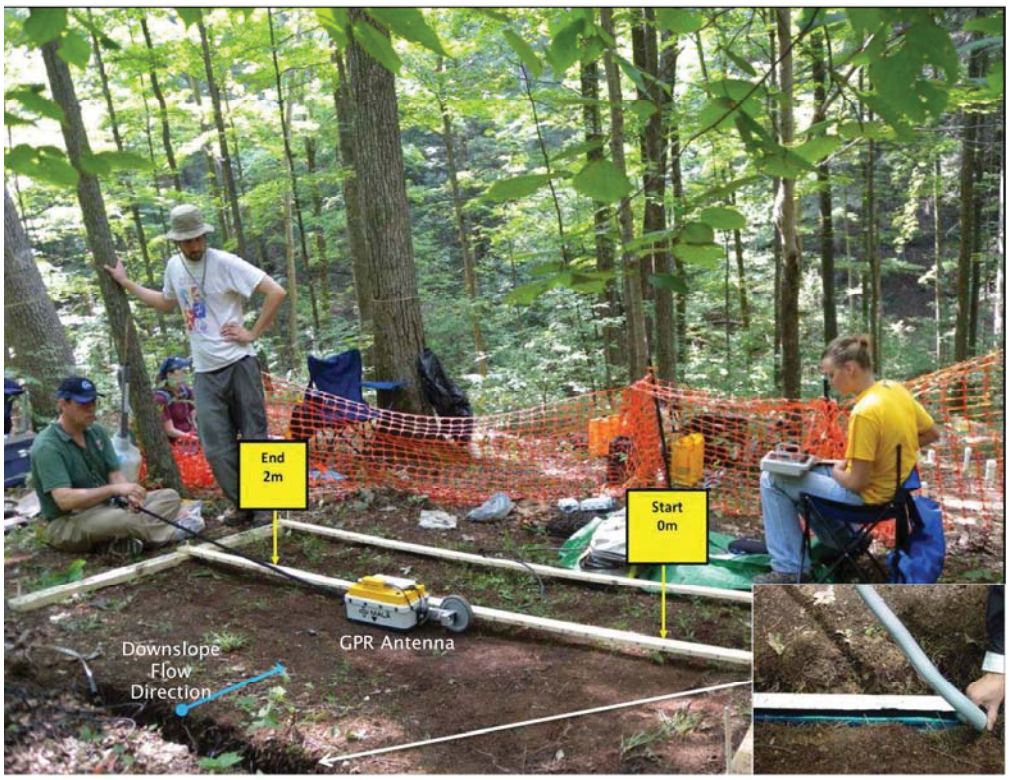

Figure 2: Water and brilliant blue dye were pumped into a shallow trench upslope of the GPR survey grid. A slotted, meter-long PVC pipe (inset) was used to ensure the tracer solution was dispersed uniformly and to maintain a constant head during the injection. An adjustable wooden frame acted as a GPR antenna guide to ensure reproducible data collection.

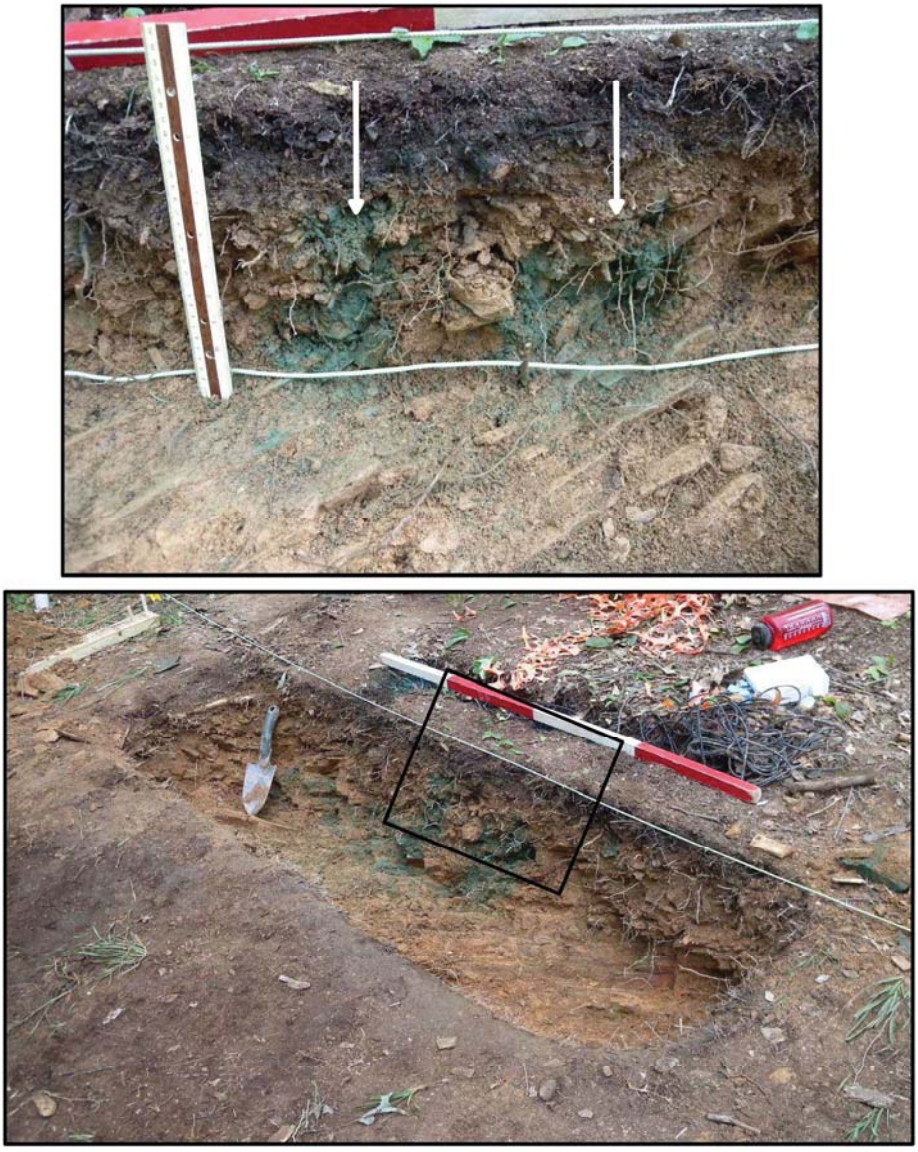

Figure 3: The top photograph shows the excavation face near the center of the injection trench to a depth of 25 cm showing two distinct fingers of dye (arrows). Rope in the photograph shows the intersection of the horizontal and vertical faces. The ruler is 30.5 cm (1 ft) long. The bottom photograph shows the infiltration trench and the final extent of the excavation, reaching a depth of 38 cm. The red and white markings on the pole are each 30.5 cm long. The black box outlines the region photographed in the enlargement above.

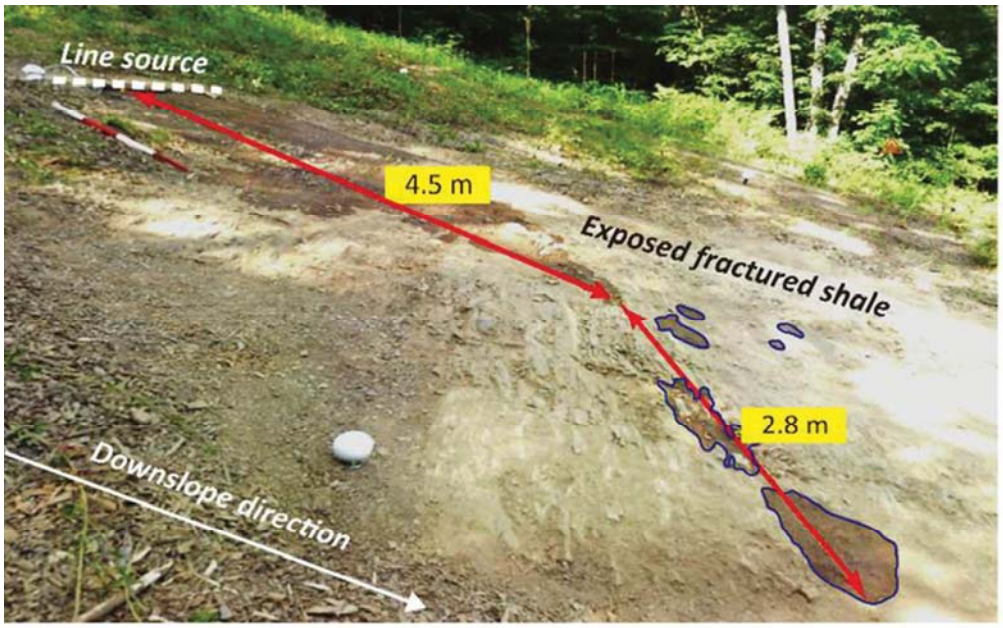

Figure 4: Photograph of soil moisture revealed in the infiltration experiment along the excavated dipslope (secondary site). Water moved laterally approximately 4.5 m until a PF was encountered. Further lateral flow may take place through the horizontal fissures in saprock and form the observed return flow at a downslope location (wet surfaces marked at 2.8 m).

59x37mm (300 x 300 DPI)

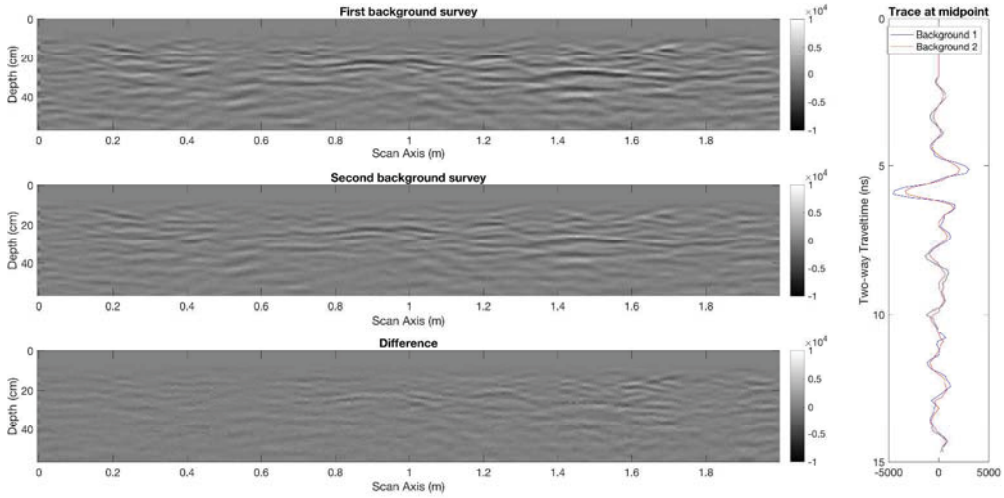

Figure 5: Comparison of the line closest to the injection trench from the two background surveys collected before injection, the differenced section, and center traces from both lines showing the reproducibility of the data. The first 2 nS (8 cm) have been muted to eliminate the air wave. Depth was calculated assuming a homogeneous velocity of 0.077 m/nS.

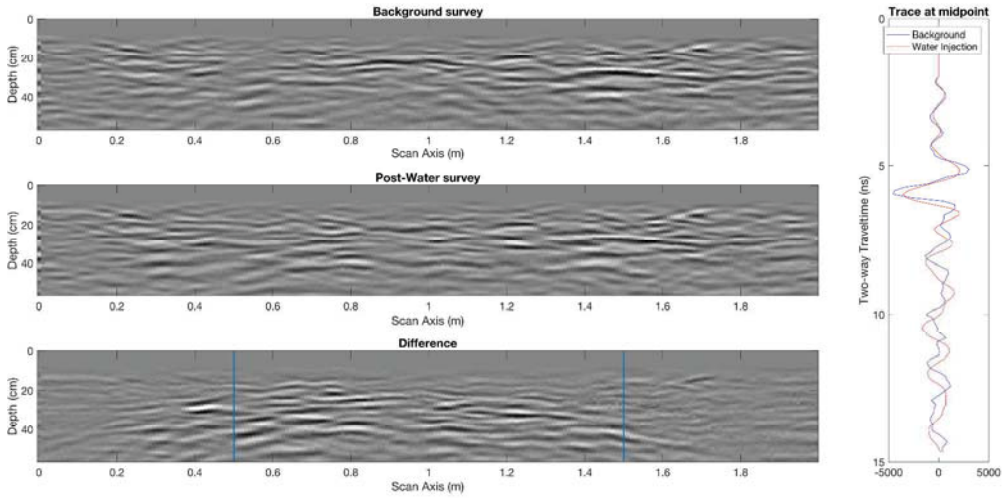

Figure 6: Comparison of the line closest to the injection trench from before and after the water injection. The differenced section shows the change starting at about 15 cm broadening with depth and trending slightly to the left, which is consistent with infiltration path seen in the excavation (Figure 3). Note that the vertical blue lines in the differenced radargram align with the ends of the injection trench with ran from 50 – 150 cm and was upslope 20 cm from this line. Change in amplitude and a slight phase shift can be seen in the sample trace from the center of the section. The first 2 nS (8 cm) have been muted to eliminate the air wave. Depth was calculated assuming a homogeneous velocity of 0.077 m/nS.

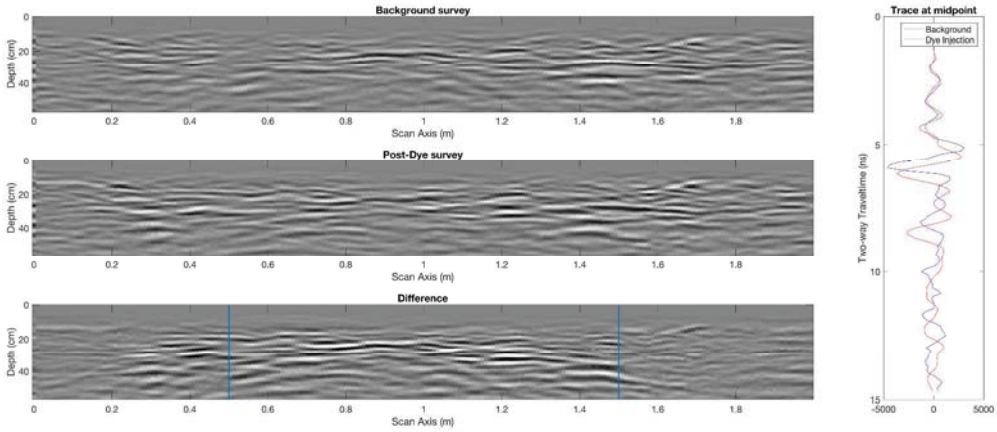

Figure 7: Comparison of the line closest to the injection trench from before and after the dye solution injection. Note that the vertical blue lines in the differenced radargram align with the ends of the injection trench with ran from 50 – 150 cm and was upslope 20 cm from this line. The change in the differenced section has slightly increased in size (compared with Figure 6). The phase shift seen in the sample trace has also increased. The first 2 nS (8 cm) have been muted to eliminate the air wave. Depth was calculated assuming a homogeneous velocity of 0.077 m/nS.

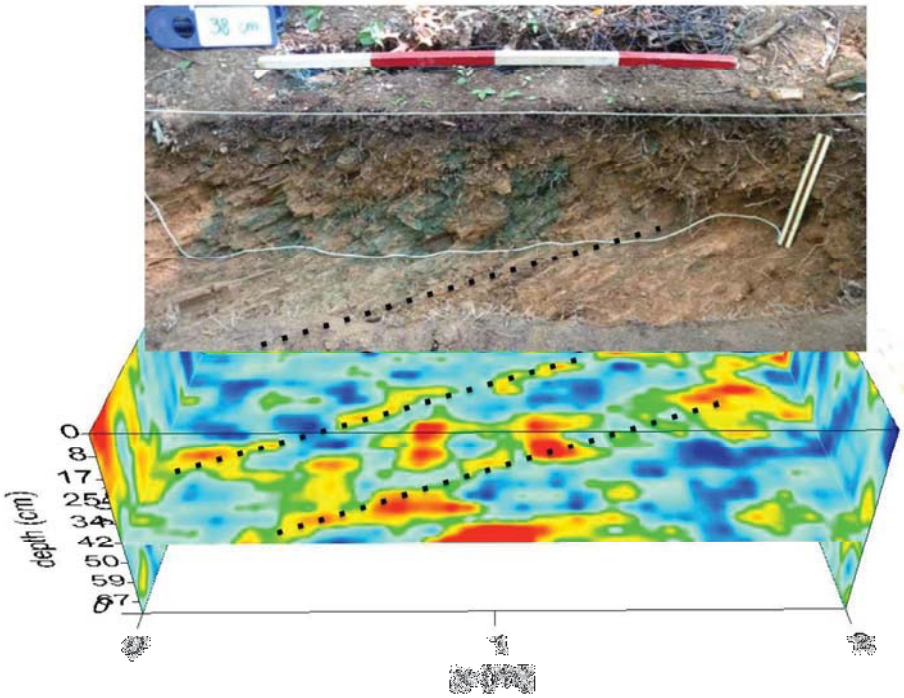

Figure 8: A horizontal slice through the 3D interpolated background GPR data at the depth of the saprock shows lineations, evidence of bedding fabric (dashed lines) that is consistent with the orientation seen in the excavation. Rope in the photograph shows the intersection of the horizontal and vertical faces.

144x108mm (300 x 300 DPI)

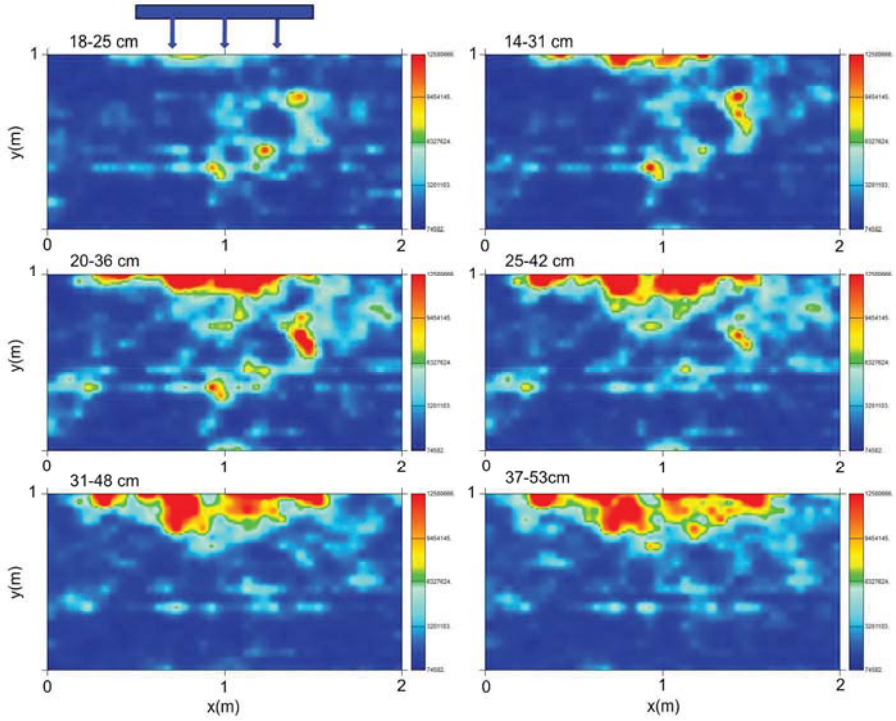

Figure 9: Horizontal slices from 8 to 53 cm made through the 3D volume at composited depths were constructed from the volume of radargrams collected after dye solution injection minus the background radargrams. The time window for each slice encompasses the return energy over roughly half a wavelength of GPR signal, with successive slices overlapping to show the change with depth. The scale is in squared amplitude. There is some indication of fingering in the radar slices, but blurred by lack of resolution and interpolation smoothing. The extent of lateral flow is clear. Most of the change is in the 20 cm of the radar grid closest to the injection trench. The trench was at 1.2 m in the y direction and extends 0.5-1.5 m in the x-direction, as shown for the upper-most slice in the top left.

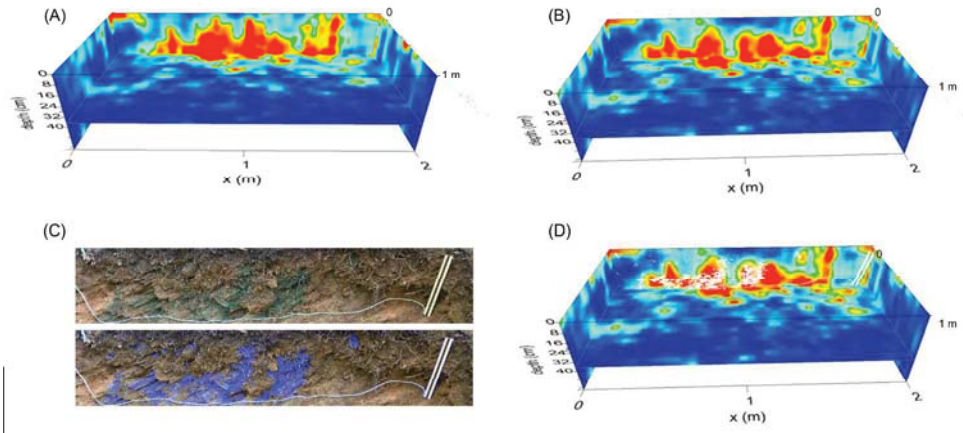

Figure 10: The radar images are a composite of a vertical x-z slice closest to the trench (0.20 m), a horizontal x-y slice at the depth equal to the base of the excavation (0.38 m), and two vertical y-z slices at the x limits of the grid. The patterns of change after the water release (A) and the dye solution release (B) are similar. The scale is normalized to the brightest reflection. The photograph of the vertical excavation face closest to the injection trench is shown (C) with and without the k-means identification of the dye stained pixels for comparison. The pixels classified as dye stained are shown superimposed on the corresponding 3D radar collected after the dye release (D) for comparison.

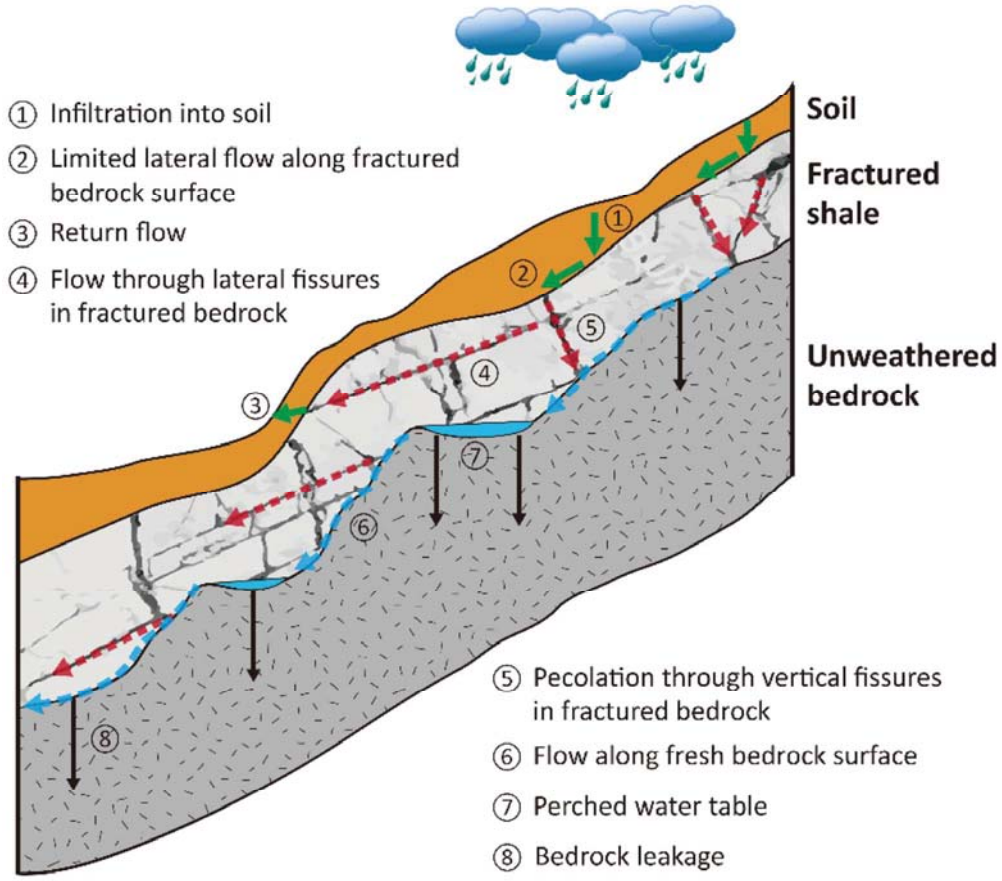

Figure 11: A refined fill-and-spill model with PF processes occurring at the top of two layers, both saprock and bedrock. In a hillslope with a thin soil cover underlain by a weathered bedrock (or saprock) layer, the bulk of the precipitation rapidly infiltrates soils and saprock and forms limited lateral PF on the soil-saprock interface. Lateral PF may take place through the horizontal fissures in saprock and form return flow at downslope. Once water encounters fresh bedrock surface, a transient water table may perch at small depressions and then triggers lateral PF downslope.